

1    **Model-based compound hypothesis testing for snATAC-seq data with PACS**

2  
3    Zhen Miao<sup>1,2</sup>, Jianqiao Wang<sup>3</sup>, Kernyu Park<sup>2</sup>, Da Kuang<sup>4</sup>, and Junhyong Kim<sup>1,2,4,†</sup>

4  
5    <sup>1</sup>Graduate Group in Genomics and Computational Biology, Perelman School of Medicine,  
6    University of Pennsylvania, Philadelphia, PA, USA

7    <sup>2</sup>Department of Biology, University of Pennsylvania, Philadelphia, PA, USA

8    <sup>3</sup>Department of Biostatistics, Harvard T.H. Chan School of Public Health, Boston, MA, USA

9    <sup>4</sup>Department Computer and Information Science, University of Pennsylvania, Philadelphia, PA,  
10    USA

11  
12    <sup>†</sup>Corresponding author

13  
14    **Correspondence:**

15    **Junhyong Kim, Ph.D.**

16    Patricia M. Williams Term Professor, Department of Biology  
17    Adjunct Professor, Department of Computer and Information Science  
18    University of Pennsylvania  
19    433 S. University Avenue  
20    Philadelphia, PA 19104

21

22 **Abstract:**

23  
24 Single nucleus ATAC-seq (snATAC-seq) experimental designs have become increasingly  
25 complex with multiple factors that might affect chromatin accessibility, including cell type, tissue  
26 of origin, sample location, batch, etc., whose compound effects are difficult to test by existing  
27 methods. In addition, current snATAC-seq data present statistical difficulties due to their sparsity  
28 and variations in individual sequence capture. To address these problems, we present a zero-  
29 adjusted statistical model, PACS, that can allow complex hypothesis testing of factors that affect  
30 accessibility while accounting for sparse and incomplete data. For differential accessibility  
31 analysis, PACS controls the false positive rate and achieves on average a 17% to 122% higher  
32 power than existing tools. We demonstrate the effectiveness of PACS through several analysis  
33 tasks including supervised cell type annotation, compound hypothesis testing, batch effect  
34 correction, and spatiotemporal modeling. We apply PACS to several datasets from a variety of  
35 tissues and show its ability to reveal previously undiscovered insights in snATAC-seq data.  
36

37 **Main:**

38  
39 Single nucleus ATAC-seq (snATAC-seq) is a powerful assay for profiling the open chromatin in  
40 individual cells<sup>1,2</sup>, and has been applied to study gene regulation across tissues and under various  
41 conditions, including homeostasis<sup>3,4,5</sup>, development<sup>6,7</sup>, or disease<sup>8,9</sup>. The cis-regulatory elements  
42 (CREs), modulated by nucleosome turnover and occupancy<sup>10</sup>, display variable accessibility across  
43 cells. The level of accessibility of CREs usually indicates its activities<sup>10</sup>, and in a cell, the activities  
44 of CREs are dynamic, dependent on various physiological factors such as cell type<sup>1,3</sup>,  
45 developmental state<sup>6,7</sup>, and spatial location of the tissue<sup>11,12</sup>. Identifying the sets of elements whose  
46 accessibility is governed by certain physiological factors is essential in understanding the cis-  
47 regulatory codes of biological processes<sup>13,14</sup>.

48  
49 Among all the factors that drive the accessibility of CREs, only some factors are experimentally  
50 controlled, for example, tissue type and location of cell collection. In a typical single cell  
51 experiment, the collection of cells is a random sample of a cell's variable states over the unknown  
52 factors (e.g., cell cycle stage, metabolic cycles) while controlling for the known factors (e.g., tissue,

53 location, batch). Here, we will call the known factors that affect or predict accessibility as  
54 independent variables following standard experimental design terminology. We note that  
55 sometimes the values of the independent variables are estimated from the data, such as  
56 unsupervised inference of cell type labels or time-sequences. Nevertheless, as the data are sampled  
57 over unknown microstates and stochastic molecular processes, the latent accessibility of a CRE  
58 should be considered as a random variable, even without experimental variability.

59

60 With the emergence of atlas-scale snATAC-seq data collection, available data usually involve  
61 multi-factorial predictive variables (e.g., health condition, donor variations, time points). A  
62 fundamental question with ATAC-seq data is whether any of the variables significantly affect or  
63 predict the accessibility of certain CREs; for example, whether cell type affects accessibility.  
64 Existing approaches for hypothesis testing typically involve pairwise testing between two states of  
65 a single factor (e.g., tests for Differential Accessible Regions, DARs, between two cell types)<sup>15,16,17</sup>.  
66 However, these approaches do not allow testing complex compound hypotheses that involve  
67 multiple independent variables. When there are multiple independent variables for a response  
68 variable, a standard approach is to model the response by a generalized linear model through an  
69 appropriate link function<sup>18</sup>. However, the standard generalized linear model (GLM) framework  
70 faces challenges in handling technical biases arising from heterogeneity in sequencing coverage  
71 of each cell and overall extreme sparsity of data. To address these limitations, we present a new  
72 statistical framework that extends the GLM framework to incorporate sample-specific missing  
73 data. Here, we derived a missing-corrected cumulative logistic regression (mcCLR) for the  
74 analysis of single cell open chromatin data. Furthermore, we utilized the Firth regularization<sup>19,20</sup>  
75 to account for data sparsity.

76

77 With this statistical framework, we present our Probability model of Accessible Chromatin of  
78 Single cells (PACS), a toolkit for snATAC-seq analysis. PACS allows methods for complex  
79 compound analysis tasks in snATAC-seq data analysis, including cell type classification, feature-  
80 level batch effect correction, and spatiotemporal data analysis. With simulated data and real data,  
81 we show that PACS effectively controls false positives while maintaining sensitivity for model  
82 testing. We apply PACS to a mouse kidney dataset, a developing human brain dataset, and a time-

83 series PBMC treatment dataset, all of which have complex study designs, to demonstrate its  
84 capability to model multiple sources of variations for hypothesis-driven biological inference.  
85

86 **Results:**

87  
88 Probabilistic model of accessible peaks and statistical test framework

89 In the PACS framework, we model the accessibility state of CREs in a single cell as a function of  
90 predictive factors such as cell type, physiological/developmental time, spatial region, etc. We use  
91 a design matrix,  $F_{C \times J}$  to represent these variables, where  $C$  is the number of cells and  $J$  is the  
92 number of independent variables (including dummy variables). Let  $Y_{C \times M}$  represent an integer-  
93 valued snATAC-seq count matrix across  $C$  cells and  $M$  genomic regions. For empirical ATAC-  
94 seq data, these regions  $M$  are determined by data-dependent peak calling, where peaks are regarded  
95 as the set of candidate CREs<sup>21,22</sup>. As snATAC-seq can recover quantitative information on the  
96 density and distribution of nucleosomes<sup>17,23</sup>, we use integer values  $Y_{cm} \in \{0,1,2, \dots\}$  to represent  
97 the level of accessibility. Existing pipelines diverge in the quantification of snATAC-seq counts,  
98 and we propose to use the paired insertion count (PIC) matrix as a uniform input for downstream  
99 analyses<sup>17</sup>. For standard snATAC-seq experiments, PIC counts follow a size-filtered signed  
100 Poisson (ssPoisson) distribution for a given Tn5 insertion rate<sup>17</sup>. Thus, the integer-valued PIC  
101 counts are observed measurements of the latent Tn5 insertion rates and chromatin accessibility  
102 (Fig. 1, upper panel). Based on this latent variable perspective we developed a proportional odds  
103 cumulative logit model to decompose the cumulative distribution of  $Y_{cm}$  by its predictive variables  
104  $F_{c*}$ .

105  
106 With cell-specific nucleosome preparation and sequencing depth, the (observed) snATAC-seq  
107 output may miss sequence information from certain accessible chromatin (**Fig. 1**, lower panel).  
108 Here, we use  $R_{C \times M}$ , with binary values, to represent the read recovery/capturing status for each  
109 cell and region. This matrix encapsulates all the experimental factors (Tn5 activities, sequencing  
110 depth, etc.) that result in a disparity of reads recovered across cells. The observed chromatin states,  
111 denoted by  $Z_{CM}$ , are specified by the element-wise product between the latent accessibility  $Y_{CM}$   
112 and the capturing status  $R_{CM}$ . Since various experimental factors such as sequencing depth are cell-  
113 specific, we further assume the capturing probability  $P(R_{cm} = 1)$  to be unique to each cell but

114 common to all peaks in that cell, and thus we use  $q_c$  to denote this conditional read capturing  
115 probability in cell  $c$ .

116  
117 Motivated by the latent variable model and to account for cell-specific missing data, we extended  
118 the cumulative logit model to simultaneously decompose accessibility as:  
119

$$\begin{aligned} 120 \text{logit}(\text{P}(Y_{cm} \geq 1)) &= \alpha^{(1)} + \sum_{j=1}^J \beta_j F_{cj}, \text{ where } \text{P}(Z_{cm} \geq 1) = \text{P}(Y_{cm} \geq 1) q_c \\ 121 \text{logit}(\text{P}(Y_{cm} \geq 2)) &= \alpha^{(2)} + \sum_{j=1}^J \beta_j F_{cj}, \text{ where } \text{P}(Z_{cm} \geq 2) = \text{P}(Y_{cm} \geq 2) q_c \\ 122 &\dots \\ 123 \text{logit}(\text{P}(Y_{cm} \geq T)) &= \alpha^{(T)} + \sum_{j=1}^J \beta_j F_{cj}, \text{ where } \text{P}(Z_{cm} \geq T) = \text{P}(Y_{cm} \geq T) q_c \end{aligned} \tag{Eq. 1}$$

124  
125  
126 where  $q_c$  is the capturing probability for a cell  $c$ ,  $\text{P}(Y_{cm} \geq t)$  is the sampling probability of cells  
127 with accessibility level greater than or equal to  $t$ ,  $\alpha^{(t)}$  is the intercept term in the  $t^{\text{th}}$  cumulative  
128 logit, and  $\beta_j$  is the coefficient for the  $j^{\text{th}}$  column of the design matrix. Eq. 1 assumes a proportional  
129 odds model, where we have a common set of coefficients  $\beta_j$  for all levels of the cumulative  
130 distribution, while allowing for a unique constant term  $\alpha^{(t)}$  for each level. Hereafter, we refer to  
131 our method as the **mcCLR** model, which stands for the missing-corrected cumulative logit  
132 regression model.

133  
134 With the formulation above, the effect of a complex set of independent variables (and their  
135 interactions) on accessibility can be tested by the null hypothesis of  $\beta_i = 0$  with a likelihood ratio  
136 test. One statistical challenge is to estimate  $q_c$ 's for each cell. We assumed the same capturing  
137 probability within a cell regardless of accessibility across different peaks such that the problem is  
138 tractable and can be computed efficiently. Operationally, we first group the cells by their  
139 combination of the treatments and then utilize a coordinate descent algorithm to obtain estimates  
140 of  $\text{P}(Y_{cm} \geq 1|f_c)$  and  $q_c$  (**Methods**).

141  
142 Another statistical challenge of snATAC-seq is that the data is very sparse, creating a so-called  
143 “perfect separation” problem (see<sup>24</sup>). Here, we developed a regularized model to resolve the issues

144 with sparsity in snATAC-seq data by generalizing the Firth logistic regression model<sup>19,25</sup>, where  
145 we incorporate the cell-specific capturing probability (Eq. 1) into the model (**Methods**).  
146 Essentially, a Firth penalty is introduced in the regression model:

147

148  $\log L^*(\boldsymbol{\beta}|\mathbf{Z}) = \log L(\boldsymbol{\beta}|\mathbf{Z}) + \frac{1}{2}\log |I(\boldsymbol{\beta})|$  (Eq. 2)

149

150 Where  $L^*$  represents the penalized likelihood,  $L$  is the likelihood of the regression model, and  $I(\boldsymbol{\beta})$   
151 is the information matrix. Derivations of the parameter estimation framework are described in the  
152 **Methods** section. With the proposed methods, we aim to control type I error more accurately and  
153 account for technical zeros (due to uneven data capturing) and sparse data. This regression-based  
154 model enables the testing of multiple covariates that jointly determine accessibility, while  
155 controlling for other covariates or confounders.

156

### 157 Application of PACS to cell type identification

158 To demonstrate the effectiveness of our model for separating the latent chromatin accessibility  
159 from the capturing probability, we evaluated three model assumptions using the task of (supervised)  
160 cell type prediction, where the goal is to predict cell types in a new snATAC-seq dataset given an  
161 annotated (labeled) dataset.

162

163 We first evaluated the accuracy of the estimation procedure of PACS. We simulated groups of  
164 cells with a spectrum of both the underlying probability of accessibility ( $P(Y_{cm} \geq 1)$ , or  $p$  in short)  
165 across peaks, and the capturing probabilities ( $q$ ) across cells (**Methods**). We then utilized PACS  
166 to jointly estimate  $p$  and  $q$ , with  $n=1000$ ,  $500$ , or  $250$  cells. The simulation results show that our  
167 estimator can determine both the capturing probabilities and open-chromatin probabilities  
168 accurately, with root mean squared errors (RMSE) for the underlying probability of accessibility  
169 from  $0.028$  ( $n=1000$ ) to  $0.027$  ( $n=250$ ) and RMSE for capturing probability from  $0.0067$  ( $n=1000$ )  
170 to  $0.012$  ( $n=250$ , **Fig. 2a-d, Supplementary Fig. 1a-b, and Supplementary Table 1**).

171

172 We next tested PACS by applying it to a cell type label transfer task, comparing it with the Naïve  
173 Bayes model. For both models, we started with an estimated  $\boldsymbol{p}_g$  for each known cell type group  
174 label  $g$ , and then applied the Bayes discriminative model to infer the most probable cell type labels

175 for novel unidentified cells. Naïve Bayes does not assume missing data; thus, it ignores the cell-  
176 specific capturing probability. The prediction performances were evaluated with ten-fold cross-  
177 validation and holdout methods, where the original cell type labels are regarded as ground truth  
178 (**Methods**). We tested the methods on five datasets, including two human cell line datasets<sup>26</sup>, two  
179 mouse kidney datasets<sup>6</sup>, and one marmoset brain dataset<sup>27</sup>. In the two human cell line datasets, the  
180 cell line labels are annotated by their SNP information<sup>26</sup>, so the labels are regarded as gold  
181 standards. For the remaining datasets, the original cell type labels are generated by clustering and  
182 marker-based annotation, so the labels may have errors.

183

184 PACS consistently outperforms the Naïve Bayes model with an average 0.31 increase in Adjusted  
185 Rand Index (ARI, **Fig. 2e**), suggesting the importance of considering the cell-to-cell variability in  
186 capturing rate. For the gold-standard cell line mixture data, we achieved almost perfect label  
187 prediction (ARI > 0.99), while Naïve Bayes had much lower accuracy with an average ARI = 0.54  
188 (**Fig. 2f-g**). For the kidney data<sup>6</sup> and the marmoset brain data<sup>27</sup>, PACS still achieved high  
189 performance, with average ARI equal to 0.92, 0.90, and 0.88 for the adult kidney, P0 kidney, and  
190 marmoset brain data, respectively. The Naïve Bayes model, on the other hand, again produced  
191 lower ARI scores, equal to 0.59, 0.65, and 0.69 for the three datasets, respectively  
192 (**Supplementary Fig. 1e-h**).

193

194 For the holdout experiment, where training and testing is done on different datasets, consistent  
195 with the above results, our method shows more accurate cell label prediction than Naïve Bayes  
196 (**Supplementary Fig. 1i**). We note that our cell type label prediction approach is very efficient,  
197 and the total time for training and prediction takes < 5 min for large datasets (>70,000 cells).

198

#### 199 PACS enables parametric multi-factor model testing for accessibility

200 Identifying the set of CREs regulated by certain physiological cues is essential in understanding  
201 functional regulation. For example, differentially accessible region (DAR) analysis tries to  
202 determine if there are cell type-specific chromosomal accessibility differences. Most snATAC-seq  
203 pipelines adopt RNA-seq differential expression methods to ask whether a peak belongs to a DAR.  
204 These approaches generally lack calibration for sparse ATAC data, and the approach of pairwise  
205 DAR tests does not allow testing more complex models that might determine peak accessibility

206 (e.g., combination of spatial location, batch effects). With existing methods for DAR detection,  
207 commonly adopted approaches are to ignore other factors or stratify by other factors to test the  
208 factor of interest, if the independent variables are nominal (e.g., cell types). However, such tests  
209 involve ad hoc partition into levels of the nominal factor and cannot test more complex models  
210 including possible metric variables (e.g., developmental time).

211  
212 To evaluate the performance of the parametric test framework in PACS, we first used simulated  
213 data to test the standard setting of a single factor model (cell types) for type I error and power, for  
214 PACS and four existing methods: ArchR<sup>26</sup>, Seurat/Signac<sup>16</sup>, snapATAC<sup>15</sup>, and Fisher's exact test.  
215 ArchR conducts the Wilcoxon rank-sum test on the subsampled cells from the initial groups, where  
216 the number of sequencing reads between two subsamples is matched. Seurat utilizes the standard  
217 logistic regression model<sup>28</sup>, but with group labels as the dependent variable and read counts and  
218 total reads as independent variables. The sparsity problem that can result in perfect separability is  
219 not resolved in this method. SnapATAC conducts a test on the pseudo-bulk data of two groups and  
220 utilizes the edgeR<sup>29</sup> regression-based test on the pseudo-bulk data with a pre-defined ad hoc  
221 variance measure (biological coefficient of variation, bvc = 0.4 for human and 0.1 for mouse data).  
222 To resemble real data, simulated samples were generated by parameterizing the model with the  
223 accessibility and capturing probability estimated directly from the human cell line dataset<sup>26</sup>.  
224 Regions with non-trivial insertion rate differences (i.e., effect size greater than 0.1) were  
225 considered to have true cell type effects, while the remaining regions were set to the same insertion  
226 rates as their average rates, and thus having no differential effect. We randomly sampled 10,000  
227 non-differential features to assess the type I error and 10,000 differential features to evaluate power,  
228 with varying numbers of cells in each group (from 250 to 1000). **Fig. 3a** shows that PACS  
229 controlled type I error at the specified level across all conditions. Among the methods that control  
230 type I error, PACS has on average 17%, 19% and 122% greater power than Fisher's exact test,  
231 ArchR and snapATAC, respectively (**Fig. 3b, Supplementary Table 2**). The reduced power of  
232 ArchR is likely due to the subsampling process, and the ad hoc "bvc" choice in snapATAC may  
233 result in a miscalibrated test with a low type I error and power. The q-q plots of the five methods  
234 are shown in **Supplementary Fig. 2a-e**.

235

236 To evaluate the performance under a multi-factor model, we next simulated another snATAC-seq  
237 dataset with two spatial locations (S1 and S2) and two cell types (T1 and T2). We introduced  
238 sample imbalance by setting S1 to contain 1600 T1 cells and 800 T2 cells, and S2 to contain 400  
239 T1 cells and 1200 T2 cells. The spatial effect term was considered to affect features both with and  
240 without cell type effects. Specifically, one-third of the features with (and without) cell type effects  
241 were assumed to also have spatial effects, with fold change in accessibility of 0.75 or 0.125. For  
242 the methods that cannot directly test effects for multiple factors, two strategies were used. The first  
243 is called the “naïve test”, where spatial location is ignored, and the test is conducted between two  
244 cell types. The second is called the “stratified test”, where we stratified the dataset by spatial  
245 location and conducted a pairwise test between cell types on each stratum, followed by using the  
246 standard Fisher combination test to combine p-values (**Methods**). Across all methods and test  
247 strategies, only snapATAC (naïve and stratified), ArchR-stratified, and PACS controlled type I  
248 error at the specified level (**Fig. 3c**); PACS remained the most powerful test and detected 7.6, 5.9,  
249 and 1.2-fold more true differential peaks compared with those identified by snapATAC-naïve,  
250 snapATAC-stratified, and ArchR-stratified, respectively (**Fig. 3d, Supplementary Table 3**).  
251

252 We then simulated a time-series dataset with five time points, to evaluate our model performance  
253 for ordinal covariates. We assumed two temporal trends of accessibility, linear and quadratic trends.  
254 To put this in a biological setting, the quadratic trend may represent the presence of an acute spike  
255 response and the linear trend may represent temporally accumulating chronic responses. The  
256 PACS framework could detect both linear and quadratic signals, and its power is dependent on the  
257 “effect sizes” defined as the log fold change of accessibility between the highest and lowest  
258 accessibility (**Fig. 3e-f**).  
259

260 We also evaluated the PACS model in real datasets. As the ground truth is unknown, we utilized  
261 a sampling-based approach. We used randomly permuted cell type labels to estimate the type I  
262 error. To evaluate power, we conducted tests on cell types and treated the consensus DAR set from  
263 all methods as “true DARs” (after type I error control, see **Methods**). For the standard two-group  
264 DAR test, our method consistently controlled type I error and achieved high power, across  
265 different datasets (**Fig. 3g-h, Supplementary Fig. 2f-i**).  
266

267 Taken together, we demonstrated with simulated and real datasets that PACS is a flexible test  
268 framework with well-calibrated test statistics.

269

270 **PACS identifies kidney cell type-specific regulatory motifs and allows direct batch correction**

271 One important feature of PACS is its ability to handle complex datasets with multiple confounding  
272 factors. To test the performance of PACS, we analyzed an adult kidney dataset with strong batch  
273 effects<sup>6</sup>. This dataset contains three samples generated independently (in three batches), and the  
274 authors identified a strong batch effect. Existing methods for batch correction map the ATAC-seq  
275 features to a latent vector space to subtract the batch effects. For example, the original study<sup>6</sup> relies  
276 on Harmony<sup>30</sup> to remove the batch effect in latent space for visualization and clustering, but the  
277 batch effect is still present in the peak feature sets, which could confound downstream analyses  
278 and inferences.

279

280 To remove the batch effect at the feature level, we assume that the batch effect will affect (increase  
281 or decrease) the accessibility of certain peaks, and these effects are orthogonal to the biological  
282 effects. This assumption is necessary for most of the existing batch-effect correction methods (e.g.,  
283 MNN<sup>31</sup>, Seurat<sup>32</sup>, and Harmony<sup>30</sup>), as a matter of experimental design. With this assumption, we  
284 applied PACS on the adult kidney data, detected significant DAR peaks among batches (P value  
285 < 0.05 with or without FDR correction) and removed batch-effect peaks from the feature set. We  
286 next implemented Signac to process the original data as well as the batch effect-corrected data,  
287 without any other batch correction steps. Dimension reductions with UMAP suggested that the  
288 original data contained a strong batch effect, where almost all cell types are separated by batch  
289 (**Fig. 4a-b**). After removing the peaks with strong batch effects, the cells are better mixed among  
290 batches (**Fig. 4c-d, Supplementary Fig. 3a-b**). Note that different cell types are still separated,  
291 suggesting the biological differences are (at least partially) maintained. Since UMAP visualization  
292 may not fully preserve the actual batch mixing structure, we adopted a batch mixing score from  
293 Ref.<sup>33</sup> to quantify the batch effect in the PCA space. The batch mixing score is defined as the  
294 average proportion of nearest neighbor cells with different batch identities, where a higher score  
295 indicates better mixing between batches, and thus a smaller batch effect (**Methods**). We  
296 normalized the mean batch mixing score by dividing it by the expected score under the random

297 mixing scenario. After batch effect correction with PACS, the normalized mean batch mixing score  
298 is 0.358 or 0.417 compared with 0.122 before batch correction.

299

300 We next applied our method to identify cell type-specific features while adjusting for batch effect.  
301 We focused on the two proximal tubule subtypes, proximal convoluted tubules (PCT) and  
302 proximal straight tubules (PST). By fitting our mcCLR model with cell type and batch effect, we  
303 identified 19,888 and 62,368 significant peaks for PCT and PST, respectively (FDR-corrected P  
304 value < 0.05, **Supplementary Tables 4-5**). The original study utilized snapATAC, which reported  
305 23,712 and 36,078 significant peaks for PCT and PST, respectively. With the batch-corrected  
306 differential peaks, we then conducted GREAT enrichment analysis<sup>34,35</sup> to identify candidate PCT-  
307 and PST-specific genes (**Supplementary Tables 6-7**). We identified *Gc*, *Nox4*, *Slc4a4*, *Bnc2*,  
308 *Slc5a12*, and *Ndrg1* genes as top PCT-enriched genes, and *Ghr*, *Gramd1b*, *Etv6*, *Atp11a*, *Gse1*,  
309 and *Sik1* as top PST-enriched genes. The associated genomic pile-up figures for the CREs of these  
310 genes are shown in **Fig. 4e**, and these findings were supported by a public scRNA-seq dataset<sup>36</sup>  
311 (**Fig. 4f**).

312

### 313 PACS dissects complex accessibility-regulating factors in the developing human brain

314 We applied our method to the human brain dataset<sup>11</sup>, which is more challenging due to the complex  
315 study design with cells collected from six donors across eight spatial locations. Substantial  
316 sequencing depth variations among samples has also been noticed, which further complicated the  
317 analysis (**Supplementary Fig. 5a-c**). To study how spatial locations affect chromatin structure,  
318 the original reference focused on the prefrontal cortex (PFC) and primary visual cortex (V1)  
319 regions, as they were the extremes of the rostral-caudal axis<sup>11</sup>. With the multi-factor analysis  
320 capacity of PACS, we conducted analyses to (1) identify the region effect, while adjusting for the  
321 donor effect, (2) identify the cell-type specific region effect.

322

323 We first examined the marginal effect of brain regions on chromatin accessibility, holding other  
324 factors constant (**Methods**). For this, we focused on a subset of three donors where spatial  
325 information is retained during data collection (**Fig. 5a-c, Supplementary Table 8**). In total, we  
326 identified 146,676 brain region-specific peaks (FDR corrected P value < 0.05). Between PFC and  
327 V1 regions, we identified 30,455 DAR peaks, ~20% more compared with the original study

328 **(Supplementary Tables 9-10).** With the region-specific DARs, we conducted motif enrichment  
329 analysis to identify region-specific TFs. For the PFC and V1 regions, we found several signals that  
330 were consistent with the original article<sup>11</sup>, including PFC-specific motifs *MEIS1*, *TBX21*, and  
331 *TBR1*, and V1-specific motifs *MEF2B*, *MEF2C*, *MEF2A*, and *MEF2D*. Moreover, we identified  
332 additional V1-specific motifs *ETS* and *ZIC2* (**Fig. 5d**), supported by the scRNA-seq data collected  
333 from the same regions<sup>37</sup>. We also noticed that some neuron development-associated TFs, including  
334 *OLIG2* and *NEUROG2*, are enriched in both brain regions but with different binding sites, likely  
335 due to different co-factors that open different DNA regions. Motif enrichment results for both brain  
336 regions are reported in **Supplementary Tables 11-12**.

337

338 Next, we used PACS to examine the location effect across different cell types along excitatory  
339 neurogenesis. This corresponds to testing the interaction terms between spatial location and cell  
340 types, while adjusting for donor effect (**Fig. 5e**). The previous study reported that the chromatin  
341 status of the intermediate progenitor cells (IPC) population started to diverge between PFC and  
342 V1 regions. Consistent with the article, we identified 2773 significant differential peaks between  
343 PFC and V1 at IPC stage, 52% more than snapATAC (**Supplementary Table 13**).

344

345 In sum, we show the implementation of PACS for data with three levels of factors: donor, spatial  
346 region, and cell type. PACS can be applied to study one factor or the interaction between factors  
347 while adjusting for other confounding factors, and test results have higher power.

348

#### 349 PACS identifies time-dependent immune responses after stimulation

350 The existing methods for DAR detection rely on pairwise comparisons, and thus are not applicable  
351 to ordinal or continuous factors. One such example is the snATAC-seq data collected at multiple  
352 time points. Here, we apply PACS to a peripheral blood mononuclear cell (PBMC) dataset  
353 collected at three time points (0h control, 1h, and 6h) after drug treatment<sup>38</sup>. Multiple treatments  
354 have been applied separately to cells collected from four human donors. While PACS can  
355 simultaneously model all drugs and conditions, we focus on the ionomycin plus phorbol myristate  
356 acetate (PMA) treatment to demonstrate the PACS workflow. The factors included in the PACS  
357 model are shown in **Fig. 6a**, where cell type and donor effects are categorical, and the time effect  
358 is coded as an ordinal variable. Note that time can be alternatively coded as a continuous variable.

359

360 We tested the treatment effect by identifying open chromatin regions that show a gradual increase  
361 or decrease in accessibility after treatment. In total, we detected 35,356 peaks with a strong  
362 treatment effect across five broad cell types (B cell, CD4 T cell, CD8 T cell, Monocyte, and NK  
363 cell, **Supplementary Tables 14-16**). Across the cell types, CD4 and CD8 T cells show the most  
364 significant changes in chromatin landscape after treatment (**Fig. 6b-c**). This is expected, as PMA  
365 can induce T cell activation and proliferation<sup>39</sup>. Among the peaks with significant PMA treatment  
366 effect, most become more accessible after treatment, consistent with the activation function of the  
367 treatment. We then conducted gene enrichment analysis with GREAT<sup>35</sup>, where we identified  
368 several GO pathways associated with T cell activation, such as “regulation of T cell differentiation”  
369 and “regulation of interleukin-2 production” (**Supplementary Table 17**). We also identified  
370 enriched genes including *DUSP5*, *IL1RL1*, *TBX21*, and *CXCR3* (**Supplementary Table 18**),  
371 expression of which have been previously reported to be up-regulated in PMA treatment<sup>40,41,42,43</sup>.  
372 Notably, *DUSP5* is known to play an essential role in the immune response through regulation of  
373 NF-κB as well as ERK1/2 signal transduction<sup>44</sup>, and *TBX21* is an immune cell TF that also directs  
374 T-cell homing to pro-inflammatory sites via regulation of *CXCR3* expression<sup>45</sup>. **Fig. 6d-e** showed  
375 the cell type-specific open chromatin landscape dynamic after the PMA treatment. We noticed that  
376 some CREs respond to the treatment effect across all cell types and some CREs become activated  
377 in only certain cell types.

378

## 379 Discussion:

380

381 Single-cell sequencing data is characterized by uneven data capturing and data sparsity. For  
382 scRNA-seq data, data normalization has been an essential step for adjusting for uneven data  
383 capturing; however, in scATAC-seq data, such a notion does not exist, which remains a challenge  
384 for data analysis. Here, PACS resolves the issue of sequencing coverage variability in scATAC-  
385 seq data by combining a probability model of the underlying group-level accessibility with an  
386 independent cell-level capturing probability. We applied PACS to tasks of (supervised) cell type  
387 annotation, showed its improved performance compared with the Naïve Bayes model that does not  
388 consider cell-specific capturing probability.

389

390 With more data being generated for different tissue conditions, atlas-level data integration is  
391 essential for understanding tissue dynamics under various conditions. The cell type annotation  
392 framework enabled us to transfer the cell type annotation from reference dataset to another dataset,  
393 which resolves one challenge in integrative data analysis. Another challenge of data integration is  
394 to jointly model various factors (e.g., cell type, spatial locations) that govern cellular CRE  
395 activities. Standard GLM framework could not address the uneven data capturing in snATAC-seq  
396 data, so we developed a statistical model that extends the standard GLM framework to account for  
397 cell-specific missing data. By utilizing this missing-corrected cumulative logistic regression  
398 (mcCLR) model with regularization, PACS can conduct multi-covariate hypothesis tests and can  
399 be used for spatial and temporal data analysis. Here we analyzed three empirical datasets from  
400 brain, kidney, and blood samples to show the utility and flexibility of our framework in large,  
401 complex datasets.

402

403 We have previously derived a parametric model of the snATAC-seq read count, called size-filtered  
404 signed Poisson distribution (ssPoisson)<sup>17</sup>. Here, we treat the insertion rate as a latent variable and  
405 directly model the paired insertion counts (PIC) of the data with an extended cumulative logistic  
406 regression model, which enabled fast and efficient computation. Future research will be conducted  
407 to explore the potential of parametric distributions. In summary, PACS allows versatile hypothesis  
408 testing for the analysis of snATAC-seq data, and its capability of jointly accounting for multiple  
409 factors that govern the chromosomal landscape will help investigators dissect multi-factorial  
410 chromatin regulation.

411

412 **References:**

- 413  
414 1. Buenrostro, J. D. *et al.* Single-cell chromatin accessibility reveals principles of regulatory  
415 variation. *Nature* **523**, 486–490 (2015).
- 416 2. Mezger, A. *et al.* High-throughput chromatin accessibility profiling at single-cell resolution.  
417 *Nat. Commun.* **9**, 3647 (2018).
- 418 3. Cusanovich, D. A. *et al.* A Single-Cell Atlas of In Vivo Mammalian Chromatin Accessibility.  
419 *Cell* **174**, 1309-1324.e18 (2018).
- 420 4. Arda, H. E. *et al.* A Chromatin Basis for Cell Lineage and Disease Risk in the Human  
421 Pancreas. *Cell Syst.* **7**, 310-322.e4 (2018).
- 422 5. Zhang, K. *et al.* A single-cell atlas of chromatin accessibility in the human genome. *Cell* **184**,  
423 5985-6001.e19 (2021).
- 424 6. Miao, Zhen *et al.* Single cell regulatory landscape of the mouse kidney highlights cellular  
425 differentiation programs and disease targets. *Nat. Commun.*  
426 doi:<https://doi.org/10.1038/s41467-021-222266-1>.
- 427 7. Cusanovich, D. A. *et al.* The cis-regulatory dynamics of embryonic development at single-cell  
428 resolution. *Nature* **555**, 538–542 (2018).
- 429 8. Satpathy, A. T. *et al.* Massively parallel single-cell chromatin landscapes of human immune  
430 cell development and intratumoral T cell exhaustion. *Nat. Biotechnol.* **37**, 925–936 (2019).
- 431 9. Corces, M. R. *et al.* Lineage-specific and single-cell chromatin accessibility charts human  
432 hematopoiesis and leukemia evolution. *Nat. Genet.* **48**, 1193–1203 (2016).
- 433 10. Klemm, S. L., Shipony, Z. & Greenleaf, W. J. Chromatin accessibility and the regulatory  
434 epigenome. *Nat. Rev. Genet.* **20**, 207–220 (2019).

- 435 11. Ziffra, R. S. *et al.* Single-cell epigenomics reveals mechanisms of human cortical  
436 development. *Nature* **598**, 205–213 (2021).
- 437 12. Deng, Y. *et al.* Spatial profiling of chromatin accessibility in mouse and human tissues.  
438 *Nature* **609**, 375–383 (2022).
- 439 13. Kim, S. & Wysocka, J. Deciphering the multi-scale, quantitative cis-regulatory code. *Mol.*  
440 *Cell* **83**, 373–392 (2023).
- 441 14. Miao, Z., Humphreys, B. D., McMahon, A. P. & Kim, J. Multi-omics integration in the age  
442 of million single-cell data. *Nat. Rev. Nephrol.* **17**, 710–724 (2021).
- 443 15. Fang, R. *et al.* Comprehensive analysis of single cell ATAC-seq data with SnapATAC. *Nat.*  
444 *Commun.* **12**, 1337 (2021).
- 445 16. Stuart, T., Srivastava, A., Madad, S., Lareau, C. A. & Satija, R. Single-cell chromatin state  
446 analysis with Signac. *Nat. Methods* **18**, 1333–1341 (2021).
- 447 17. Miao, Z. & Kim, J. Is single nucleus ATAC-seq accessibility a qualitative or quantitative  
448 measurement? *bioRxiv* 2022.04.20.488960 (2022) doi:10.1101/2022.04.20.488960.
- 449 18. Agresti, A. *Foundations of linear and generalized linear models*. (John Wiley & Sons,  
450 2015).
- 451 19. FIRTH, D. Bias reduction of maximum likelihood estimates. *Biometrika* **80**, 27–38 (1993).
- 452 20. Heinze, G. A comparative investigation of methods for logistic regression with separated or  
453 nearly separated data. *Stat. Med.* **25**, 4216–4226 (2006).
- 454 21. Moore, J. E. *et al.* Expanded encyclopaedias of DNA elements in the human and mouse  
455 genomes. *Nature* **583**, 699–710 (2020).
- 456 22. Li, Y. E. *et al.* An atlas of gene regulatory elements in adult mouse cerebrum. *Nature* **598**,  
457 129–136 (2021).

- 458 23. Martens, L. D., Fischer, D. S., Theis, F. J. & Gagneur, J. Modeling fragment counts  
459 improves single-cell ATAC-seq analysis. 2022.05.04.490536 Preprint at  
460 <https://doi.org/10.1101/2022.05.04.490536> (2022).
- 461 24. Agresti, A. *Categorical data analysis*. vol. 792 (John Wiley & Sons, 2012).
- 462 25. Heinze, G. & Schemper, M. A solution to the problem of separation in logistic regression.  
463 *Stat. Med.* **21**, 2409–2419 (2002).
- 464 26. Granja, J. M. *et al.* ArchR is a scalable software package for integrative single-cell chromatin  
465 accessibility analysis. *Nat. Genet.* **53**, 403–411 (2021).
- 466 27. Bakken, T. E. *et al.* Comparative cellular analysis of motor cortex in human, marmoset and  
467 mouse. *Nature* **598**, 111–119 (2021).
- 468 28. Ntranos, V., Yi, L., Melsted, P. & Pachter, L. A discriminative learning approach to  
469 differential expression analysis for single-cell RNA-seq. *Nat. Methods* **16**, 163–166 (2019).
- 470 29. Chen, Y., Lun, A. T. L. & Smyth, G. K. From reads to genes to pathways: differential  
471 expression analysis of RNA-Seq experiments using Rsubread and the edgeR quasi-likelihood  
472 pipeline. Preprint at <https://doi.org/10.12688/f1000research.8987.2> (2016).
- 473 30. Korsunsky, I. *et al.* Fast, sensitive and accurate integration of single-cell data with Harmony.  
474 *Nat. Methods* **16**, 1289–1296 (2019).
- 475 31. Haghverdi, L., Lun, A. T. L., Morgan, M. D. & Marioni, J. C. Batch effects in single-cell  
476 RNA-sequencing data are corrected by matching mutual nearest neighbors. *Nat. Biotechnol.*  
477 **36**, 421–427 (2018).
- 478 32. Stuart, T. *et al.* Comprehensive Integration of Single-Cell Data. *Cell* **177**, 1888–1902.e21  
479 (2019).

- 480 33. Chari, T. & Pachter, L. *The Specious Art of Single-Cell Genomics*.  
481 <http://biorxiv.org/lookup/doi/10.1101/2021.08.25.457696> (2021)  
482 doi:10.1101/2021.08.25.457696.
- 483 34. McLean, C. Y. *et al.* GREAT improves functional interpretation of cis-regulatory regions.  
484 *Nat. Biotechnol.* **28**, 495–501 (2010).
- 485 35. Tanigawa, Y., Dyer, E. S. & Bejerano, G. WhichTF is functionally important in your open  
486 chromatin data? *PLOS Comput. Biol.* **18**, e1010378 (2022).
- 487 36. Ransick, A. *et al.* Single-Cell Profiling Reveals Sex, Lineage, and Regional Diversity in the  
488 Mouse Kidney. *Dev. Cell* **51**, 399–413.e7 (2019).
- 489 37. Nowakowski, T. J. *et al.* Spatiotemporal gene expression trajectories reveal developmental  
490 hierarchies of the human cortex. *Science* **358**, 1318–1323 (2017).
- 491 38. Kartha, V. K. *et al.* Functional inference of gene regulation using single-cell multi-omics.  
492 *Cell Genomics* **2**, 100166 (2022).
- 493 39. Ai, W., Li, H., Song, N., Li, L. & Chen, H. Optimal Method to Stimulate Cytokine  
494 Production and Its Use in Immunotoxicity Assessment. *Int. J. Environ. Res. Public. Health*  
495 **10**, 3834–3842 (2013).
- 496 40. Brignall, R. *et al.* Integration of Kinase and Calcium Signaling at the Level of Chromatin  
497 Underlies Inducible Gene Activation in T Cells. *J. Immunol.* **199**, 2652–2667 (2017).
- 498 41. Shin, H.-J., Lee, J.-B., Park, S.-H., Chang, J. & Lee, C.-W. T-bet expression is regulated by  
499 EGR1-mediated signaling in activated T cells. *Clin. Immunol.* **131**, 385–394 (2009).
- 500 42. Dagan-Berger, M. *et al.* Role of CXCR3 carboxyl terminus and third intracellular loop in  
501 receptor-mediated migration, adhesion and internalization in response to CXCL11. *Blood*  
502 **107**, 3821–3831 (2006).

- 503 43. Cooke, M. *et al.* Differential Regulation of Gene Expression in Lung Cancer Cells by  
504 Diacyglycerol-Lactones and a Phorbol Ester Via Selective Activation of Protein Kinase C  
505 Isozymes. *Sci. Rep.* **9**, 6041 (2019).
- 506 44. Seo, H. *et al.* Dual-specificity phosphatase 5 acts as an anti-inflammatory regulator by  
507 inhibiting the ERK and NF- $\kappa$ B signaling pathways. *Sci. Rep.* **7**, 17348 (2017).
- 508 45. Stolarszyk, E., Lord, G. M. & Howard, J. K. The immune cell transcription factor T-bet.  
509 *Adipocyte* **3**, 58–62 (2014).
- 510 46. Winship, C. & Mare, R. D. Regression Models with Ordinal Variables. *Am. Sociol. Rev.* **49**,  
511 512 (1984).
- 512 47. Christensen, R. H. B. *Sensometrics: Thurstonian and Statistical Models*. (Technical  
513 University of Denmark, 2012).
- 514 48. Venzon, D. J. & Moolgavkar, S. H. A Method for Computing Profile-Likelihood-Based  
515 Confidence Intervals. *Appl. Stat.* **37**, 87 (1988).
- 516 49. Adey, A. C. Tagmentation-based single-cell genomics. *Genome Res.* **31**, 1693–1705 (2021).
- 517 50. Duttke, S. H., Chang, M. W., Heinz, S. & Benner, C. Identification and dynamic  
518 quantification of regulatory elements using total RNA. *Genome Res.* (2019)  
519 doi:10.1101/gr.253492.119.
- 520 51. Hao, Y. *et al.* Integrated analysis of multimodal single-cell data. *Cell* **184**, 3573–3587.e29  
521 (2021).

524 **Methods**

525 Data availability

526 We downloaded the following snATAC-seq datasets from public repositories:

527 mouse kidney data<sup>6</sup> (GEO GSE157079,

528 <https://www.ncbi.nlm.nih.gov/geo/query/acc.cgi?acc=GSE157079>),

529 human cell line data<sup>26</sup> (GEO GSE162690,

530 <https://www.ncbi.nlm.nih.gov/geo/query/acc.cgi?acc=GSE162690>),

531 developing human brain data<sup>11</sup> (GEO GSE163018,

532 <https://www.ncbi.nlm.nih.gov/geo/query/acc.cgi?acc=GSE163018>),

533 marmoset brain data<sup>27</sup> (the Brain Cell Data Center RRID SCR\_017266; <https://biccn.org/data>),

534 human PBMC time-series stimulation data<sup>38</sup> (GEO GSE178431,

535 <https://www.ncbi.nlm.nih.gov/geo/query/acc.cgi?acc=GSE178431>).

536

537 Probabilistic model of underlying open chromatin status

538 Here we model the activity of regulatory elements in each cell type group by the cumulative  
539 distribution of the accessibility. The underlying accessibility for a CRE is a function of nucleosome  
540 density and turnover rate. As we discuss in the main text, for a particular cell group, the chromatin  
541 state should be regarded as a random variable as they are sampled from mixtures of hidden  
542 microstates. Here, we expanded the model of accessible chromatin from Ref<sup>17</sup>. Briefly, let  $F_{C \times J}$  be  
543 a design matrix that summarizes known independent variables (e.g., cell type, developmental time,  
544 sample locations, etc.) across  $C$  cells,  $Y_{C \times M}$  be the underlying (latent) chromatin status across  $C$   
545 cells and  $M$  regions, where each element represent the accessibility of a genomic region. The goal  
546 of PACS is to decompose the (complementary) cumulative distribution of  $Y_{cm}$ , i.e., the series of  
547 distributions:

548

549  $P\{Y_{cm} \geq t\} = \sum_{i=t}^T \pi_i$  for  $t = 1, 2, \dots, T$       (Eq. 3)

550

551 by predictive independent variables in  $F_{c*}$ . Here the maximum value of accessibility we account  
552 for,  $T$ , is feature specific. To be precise, for a feature  $m$ ,  $T$  is the largest integer such that  
553  $\sum_c 1(Z_{cm} \geq t) \geq n_c$  where  $n_c$  is a hyperparameter. In our study,  $n_c$  is set to be  $0.25C$  but based  
554 on our evaluation, our model is not sensitive to the choice of  $n_c$ .

555

556 Model for capturing probability of cell

557 Due to various experimental factors like enzyme activity and sequencing depth disparities across  
558 cells, we introduce  $R_{C \times M}$  as a matrix representing the capturing status of each cell and region. Let  
559  $Z_{C \times M}$  be the (observed) scATAC dataset, we have  $Z = Y \otimes R$ , where  $\otimes$  denote element-wise  
560 Product. We consider  $R_{cm}$  to be sampled from a Bernoulli distribution parameterized by  $q_c$ , cell-  
561 specific capturing probability:

562

563  $R_{cm} \sim \text{Bernoulli}(q_c)$  (Eq. 4)

564

565 Joint parameter estimation for single-factor scenario

566 Given a class of data that correspond to a combination of levels of independent variables, we  
567 follow the same parameter estimation framework as described in Ref<sup>17</sup>. Briefly, assume we have  
568 a genomic region-by-cell (i.e., peak-by-cell) matrix  $Z_{C_f \times M}$  with  $C_f$  denoting the subset of cells  
569 corresponding to some combination of the independent prediction factors. The observed values in  
570  $Z_{C_f \times M}$  are ordinal values, but as most of the non-zero scATAC-seq counts are one  
571 (typically >70%), we focus on  $P(Y_{C_f m} \geq 1)$  for purposes of  $q_c$  estimation. Hereafter, we use the  
572 notation  $p_{C_f m}^{(1)}$  to represent the (non-zero) open probability of group  $C_f$  and feature  $m$ . We have  
573 further assumed  $q_c$  to be identical across different levels of accessibility for a given cell. Due to  
574 the data sparsity and the predominant counts of one, this assumption is moderate, and the  
575 estimation process will be greatly accelerated with this assumption. We use moment estimator with  
576 a coordinate descent algorithm to iteratively update  $p_{C_f m}^{(1)}$  given  $q_c$ , and update  $q_c$  given  $p_{C_f m}^{(1)}$ .

577 Briefly, we execute the following iteration until convergence:

578 1. Start with an initial estimate of  $p_m^{[0]}$

579 2. For  $t = 1, 2, \dots$

580     a. Compute  $q_c^{[t]}$  by:

581         
$$q_c^{[t]} = \frac{\sum_{m=1}^M I(z_{cm} \geq 1)}{\sum_{m=1}^M p_m^{[t-1]}}$$
 for  $c \in C_f$

582     b. Update  $p_m^{[t]}$  by moment estimator:

583 
$$p_m^{[t]} = \frac{\sum_{c \in C_f} I(z_{cm} \geq 1)}{\sum_{c \in C_f} q_c^{[t]}} \text{ for } m \in \{1, 2, \dots, M\}$$

584  
585 where we use superscript  $[t]$  to represent the  $t^{\text{th}}$  iteration, and we omit the subscript  $C_f$  and  
586 superscript  $(1)$  for  $p_{C_f m}^{(1)}$ .

587  
588 *Uniqueness of parameter estimation*  
589 In order for the above joint parameter estimation framework to converge and for the estimated  
590 parameters to be uniquely defined, there should be  $q_c = 1$  for some cells and  $p_{C_f m}^{(1)} = 1$  for some  
591 features. In PACS, we conduct a convergence check by requiring a certain proportion of cells  
592 (default 10%) to have an estimated capturing probability greater than 0.9. In the case of a cluster  
593 of cells being rare or not sufficiently deeply sequenced, the estimates may be unstable, and we  
594 recalibrate the estimates for this rare cluster to its most similar cluster to prevent potential false  
595 positives. Specifically, let  $C_{f1}$  index the rare group of cells; then, to identify the cell groups with  
596 the most similar open chromatin profile, we compute the correlation between  $p_{C_{f1}*}^{(1)}$  and  $p_{C_{fj}*}^{(1)}$  for  
597 all other clusters  $j = 1, \dots, J$ , across all regions. Assuming  $C_{fn}$  has the most similar chromatin  
598 profile, we rescale the current estimation of  $p_{C_{f1} m}^{(1)}$  by the following formula:

599  
600 
$$S = \sum_m p_{C_{fn} m}^{(1)} / \sum_m p_{C_{f1} m}^{(1)}$$
  
601 
$$p_{C_{f1}*}^{(1)'} = p_{C_{f1}*}^{(1)} \times S \quad (\text{Eq. 5})$$

602  
603 where  $S$  is the scale factor,  $p_{C_{f1} m}^{(1)'}$  is the rescaled open probability estimate for the cluster  $C_{f1}$  and  
604 feature  $m$ , and through rescaling, we are essentially assuming that most peaks are not differentially  
605 accessible between these two cell types.

606  
607 *Cell type label prediction framework*

608 Given a reference dataset, we estimate the probability of open chromatin  $p_{C_g m}^{(1)}$  for each cell type  
609  $g \in \{1, \dots, G\}$ , using the formula above. With a new set of observations  $Z'_{C' \times M}$ , we apply the Bayes  
610 discriminative model to predict the corresponding cell type labels,  $h(Z'_{c*})$ .

611

612

$$\begin{aligned} P(h(Z'_{c*}) = g | Z'_{c*}) &= P(Z'_{c*} | h(Z'_{c*}) = g) P(h(Z'_{c*}) = g) \\ &= P(h(Z'_{c*}) = g) \prod_{m=1}^M \left( p_{C_g m}^{(1)} q_c \right)^{Z'_{cm}} \left( 1 - p_{C_g m}^{(1)} q_c \right)^{1-Z'_{cm}} \quad (\text{Eq. 6}) \end{aligned}$$

614

615 where  $P(h(Z'_{c*}) = g | Z'_{c*})$  represents the posterior probability of cell  $c$  being sampled from cell  
616 group  $g$ ,  $P(Z'_{c*} | h(Z'_{c*}) = g)$  represents the conditional probability of observing  $Z'_{c*}$  given that the  
617 cell  $c$  is sampled from cell type  $g$ ,  $P(h(Z'_{c*}) = g)$  is the prior probability of a new observation  
618 belonging to cell group  $g$ , which can either be assumed to be a non-informative Dirichlet prior  
619  $\text{Dirich}(\delta)$  or estimated based on the cell type composition in reference data. Note that we have a  
620 large feature space so this choice will not make a big difference.

621

622 Missing-corrected cumulative logistic regression (mcCLR)

623 Due to high sparsity of scATAC-seq data, perfect separability is common, hindering the parameter  
624 estimation in (Eq. 1). To address this issue, we incorporated Firth regularization (Eq. 2). Here we  
625 summarize the (unregularized) log likelihood function and information matrix for the cumulative  
626 response model and derive the analytical expression for the binary model. The loss function when  
627 considering cumulative response is

628

629  $\log L(\Pi, \mathbf{y} | \mathbf{q}) = \sum_{c=1}^C \sum_{t=0}^T \log (\tilde{\pi}_{ct}) I(z_c = t) \quad (\text{Eq. 7})$

630

631 where  $C$  represent the total number of cells,  $\pi_{ct}$  and  $\tilde{\pi}_{ct}$  represent the probability of  $t$  PIC counts  
632 in cell  $c$  before and after accounting for cell-specific capturing probability, respectively.  
633 Specifically,  $\pi_{ct} = P(y_c \geq t) - P(y_c \geq t + 1)$ ,  $\Pi_c = (\pi_{c0}, \pi_{c1}, \pi_{c2}, \dots, \pi_{cT})^{\text{Trans}}$  and  $\tilde{\Pi}_c =$   
634  $Q_c \Pi_c$ , where  $Q_c$  is the capturing probability matrix of dimension  $(T + 1) \times (T + 1)$  specified as

635

636    
$$Q_c = \begin{bmatrix} 1 & 1 - q_c & 1 - q_c & \dots & 1 - q_c \\ 0 & q_c & 0 & & \\ 0 & 0 & q_c & & \vdots \\ \vdots & & & \ddots & \\ 0 & \dots & & & q_c \end{bmatrix} \quad (\text{Eq. 8})$$

637

638    In our PACS model, an approximated estimation of parameters in the cumulative logit model were  
 639    obtained using a method described in a previous set of studies<sup>46,47</sup> that based on stacking the data  
 640    and optimize with binary logistic regression specified by

641

642     $\log L(\boldsymbol{p}, \mathbf{z} | \boldsymbol{q}) = \sum_{c=1}^C [z_c \log(p_c q_c) + (1 - z_c) \log(1 - p_c q_c)] \quad (\text{Eq. 9})$

643     $I(\boldsymbol{\beta}) = F^T W F \text{ where } W = \text{diag}\left\{\frac{p_c q_c (1-p_c)^2}{1-p_c q_c}\right\} \quad (\text{Eq. 10})$

644

645    where  $p_c = P(z_c = 1)$ .

646

647    Parameter estimation for mcCLR

648    We implemented both Newton's method and the Iterative Reweighted Least Squares method  
 649    (IRLS) for parameter estimation. Briefly, for Newton's method,  $\boldsymbol{\beta}$  is estimated through the  
 650    following iteration

651

652     $\boldsymbol{\beta}^{(s+1)} = \boldsymbol{\beta}^{(s)} + I'^{-1}(\boldsymbol{\beta}^{(s)}) U^*(\boldsymbol{\beta}^{(s)}) \quad (\text{Eq. 11})$

653

654    where the superscript  $s$  represents the iteration,  $I' = I$  for the full model and  $I' = I_{-\{d\}}$  for the null  
 655    model of  $\beta_{\{d\}} = 0$ . The score function  $U^*(\beta)$  is given by:

656

657    
$$U^*(\beta_r) = U(\beta_r) + \frac{1}{2} \text{trace} \left[ I(\boldsymbol{\beta})^{-1} \frac{\partial I(\boldsymbol{\beta})}{\partial \beta_r} \right]$$
  
 658     $= \sum_{c=1}^C \frac{x_{cr}(y_c - p_c q_c)(1-p_c)}{1-p_c q_c} + \frac{1}{2} \sum_{c=1}^C f_{cr} k_r h_r, \quad (r = 1, \dots, p) \quad (\text{Eq. 12})$

659

660    where the  $h_c$ 's are the  $c^{\text{th}}$  diagonal elements of the "hat" matrix,  $H = W^{1/2} F (F^T W F)^{-1} F^T W^{1/2}$ ,  
 661    and  $k_c = (2p_c^2 q_c - 3p_c + 1) / (1 - p_c q_c)$ .

662

663 For the IRLS method, the information matrix  $I$  is replaced with an estimate of the information  
664 matrix,  $\tilde{I}$ ,

665

666 
$$\tilde{I}(\beta) = F^T \tilde{W} F, \text{ where } \tilde{W} = \text{diag}\left\{-\frac{[-p_c^2 q_c^2 + q_c(2p_c + z_i - 1) - z_i] p_c (1-p_c)}{(1-p_c q_c)^2}\right\} \quad (\text{Eq. 13})$$

667

668 Hypothesis testing framework of mcCLR

669 We utilized a generalized likelihood ratio test framework for hypothesis testing with the mcCLR  
670 model, although a Wald-type test can also be derived. As the model contains Firth regularization,  
671 we used the profile penalized likelihood approach to obtain P values<sup>25,48</sup>. Specifically, in the null  
672 model, the coefficients of interest are set to zero but still left in the model, so that the regularization  
673 accounts for the presence of these parameters during optimization.

674

675 Data simulation for single factor differential test

676 To mimic real data, we estimated insertion rates ( $\lambda_{C_f m}$ ) and  $q_c$  from the human cell line data and  
677 use these values to construct simulated data. Briefly, because viable snATAC-seq reads come from  
678 two adjacent Tn5 insertion events that have the right primer configuration (reviewed in<sup>49</sup>), we  
679 derived the size-filtered signed Poisson (ssPoisson) distribution to model this data generation  
680 process<sup>17</sup>. With the observed counts, we estimated the insertion rate parameters for two cell types,  
681 and regions with true open probability difference greater than 0.05 were set to be as true differential  
682 ( $H_a$ ) and the remaining region's open probabilities were set equal (by taking the mean) and  
683 therefore non-differential ( $H_0$ ). Based on parametric model of latent and observed accessibility,  
684 we first sampled the latent ATAC reads by ssPoisson( $\hat{\lambda}_{C_f m}$ ) for  $f = 1, 2$ , and then sampled the  
685 observing status by Bernoulli distribution parameterized by  $q_c$ . The observed data were generated  
686 by the element-wise product of these two matrices. We randomly sampled 10,000 non-differential  
687 features to assess the type I error and 10,000 differential features to evaluate power. This  
688 simulation was conducted under varying numbers of cells in each group (from 250 to 1000), and  
689 each scenario was repeated 5 times.

690

691 Data simulation for multi-factor differential test

692 Building upon the single factor setting, we further assumed the data to contain two cell types (T1  
693 and T2) being sampled from two spatial locations (S1 and S2). The goal was to infer cell-type-  
694 specific differential features while accounting for the spatial effect. We introduced sample  
695 imbalance as frequently seen in real datasets. To be precise, we considered that S1 contained 1600  
696 T1 cells and 800 T2 cells, while S2 contained 400 T1 cells and 1200 T2 cells. The spatial effect  
697 was considered to affect features both with and without a cell type effect. Specifically, a third of  
698 the features with (and without) a cell type effect showed an accessibility difference across batches,  
699 with a fold change of 0.75 or 0.125. The peak by cell count data generation procedure is the same  
700 as for the single factor setting.

701

#### 702 Data simulation for time-series differential test

703 To evaluate model performance in situations where the design matrix contains ordinal covariates,  
704 we simulated time-series snATAC-seq data across five time points. We assumed linear and  
705 quadratic temporal effects on accessibility and set the effect size (log fold change) to be 0.3 or 0.5  
706 between the two groups. The baseline accessibility was generated from the cell line data and the  
707 peak by cell count data generation procedure is the same as for the single factor setting.

708

#### 709 Evaluating type I error and power in real datasets

710 To estimate type I error in real data where the ground truth is unknown, we used a label  
711 permutation approach, where the data in one cell type were divided randomly into two groups, and  
712 a differential test was conducted between these groups. As this is randomly assigned, all features  
713 were believed to be non-DAR, so the proportion of P values smaller than 0.05 is the empirical type  
714 I error using real data. Then, we set the fifth rank percentile as the correct critical value for those  
715 methods with type I errors greater than 0.05. We next conducted a test with two different cell types  
716 using the calibrated critical values for each method. Since we do not know the true DAR set, we  
717 defined the pseudo-true DAR peaks as the union DAR set of all tested methods, using their  
718 corresponding new critical values. Power for each method was then calculated by the number of  
719 DARs detected divided by the number of pseudo-true DARs. This approach is adopted from Ref.<sup>17</sup>.

720

#### 721 Estimating effect size (fold change and accessibility change)

722 A common practice to determine differential features in single cell data is by setting a cutoff for  
723 both P value and fold change. In scRNA-seq data analysis, one way to estimate the effect size of  
724 a particular variable (predictor) is by calculating the fold change (FC) for the normalized data,  
725 obtained by dividing the normalized mean expression of one group by the other group. However,  
726 with snATAC-seq data, there is no direct normalization method available, and computing the fold  
727 change on raw read counts may lead to inaccuracies due to disparities in data capture. Here, we  
728 propose to use the capturing probability-adjusted count to compute fold change (FC) or the  
729 arithmetic difference between accessibility (accessibility change, AC) of two cell types. To be  
730 precise:

731

732 
$$FC = \frac{\sum_{c \in C_1} Z_{cm}/q_c}{\sum_{c \in C_2} Z_{cm}/q_c}, \quad AC = \sum_{c \in C_1} Z_{cm}/q_c - \sum_{c \in C_2} Z_{cm}/q_c \quad (\text{Eq. 14})$$

733

734 where  $m$  is the feature of interest and  $C_1$  and  $C_2$  are the lists of cells that contain foreground and  
735 background cell types.

736

### 737 Processing kidney adult data with Signac

738 We used Signac<sup>16</sup> to evaluate the effectiveness of our method in correcting for batch effect at the  
739 feature level. We follow the standard workflow as recommended in the Signac vignette  
740 ([https://stuartlab.org/signac/articles/pbmc\\_vignette.html](https://stuartlab.org/signac/articles/pbmc_vignette.html)). Briefly, we used the TF-IDF approach  
741 without feature selection (*min.cutoff* = ‘q0’), followed by SVD to reduce dimensionality. We then  
742 conduct clustering and UMAP visualization using the dimensions 2 to 30 (as the first LSI  
743 dimension usually reflects sequencing depth, per the Seurat tutorial). The sample and cell type  
744 labels are retrieved from the annotations in the initial publication.

745

### 746 Batch mixing score calculation

747 We calculated the batch mixing scores in the PCA space as a measure of batch effect. At the cell  
748 level, the batch mixing score is adopted from Ref.<sup>33</sup> and is defined as the proportion of nearest  
749 neighbor cells with different batch identities, where a higher score indicates better mixing between  
750 batches, and thus a smaller batch effect. At the whole data level, the batch mixing score is defined  
751 as the mean batch mixing score across all cells. To calculate the expected batch mixing score for  
752 a given dataset when no batch effect is present, let  $M$  denote a cell type-by-batch matrix, with each

753 element  $m_{ij}$  representing the number of cells in the cell type  $i$  and batch  $j$ . Then the expected data-  
754 level batch mixing score in the setting of no batch effect is given by  
755

$$756 E[\text{batch mixing score}] = \frac{1}{\sum_{i,j} m_{ij}} \left\{ \sum_i \left[ \sum_j m_{ij} \left( \frac{\sum_{k \neq j} m_{ik}}{\sum_k m_{ik}} \right) \right] \right\} \quad (\text{Eq. 15})$$

757  
758 The normalized batch mixing score is the batch mixing score divided by the expected score under  
759 random mixing, and thus a higher normalized batch mixing score indicates better mixing across  
760 samples.  
761

#### 762 Processing developing human brain data

763 This dataset contains 18 specimens collected from human donors. For our study, we excluded  
764 samples with unknown spatial locations (GW17, GW18, GW21) or samples not from the cortex  
765 (MGE\_GW20 and MGE\_twin34). Here we focused on the excitatory neuron lineage, including  
766 radial glia (RG), intermediate progenitor cells (IPCs), early excitatory neurons (earlyEN), deep  
767 layer excitatory neurons (dlENs), and upper layer excitatory neurons (ulENs). We further excluded  
768 the insular region for having too few cell counts (645 cells across five cell types). The data matrix  
769 was saved as a binary matrix, so we implemented the missing-corrected logistic regression model  
770 for the analyses of this data.  
771

#### 772 DAR identification in the developing human brain data

773 We constructed two models to identify the significant region effect of the excitatory neuron lineage.  
774 Specifically, to identify the region effect, the systematic component of the PACS model is  
775 specified as:  
776

$$777 \alpha + \sum_{k=2}^K \gamma_k 1(G_c = g_k) + \sum_{l=2}^L \zeta_l 1(S_c = S_l) + \sum_{m=2}^M \tau_m 1(D_c = D_m) \quad (\text{Eq. 16})$$

778  
779 where  $G$  is the index of cell type,  $S$  is the index of spatial location, and  $D$  is the index of the donor.  
780 The null hypothesis for the test is  $H_0: \zeta = 0$ . To identify the cell type specific region effect, we  
781 additionally included the interaction terms between each cell type and spatial location, and the test  
782 was conducted for each interaction term.

783

784 Motif enrichment analysis

785 The motif enrichment analysis was conducted with Homer<sup>50</sup>. The list of significant DAR peaks is  
786 used as input for the analysis, with the size of the search region specified as 300 bp around the  
787 peak center. The reported motif enrichment scores are FDR-corrected P values from the known  
788 motif results.

789

790 DAR identification in the human PBMC treatment data

791 To identify the cell type-specific temporal effect in the PBMC treatment data, the systematic  
792 component of the PCAS model is specified as:

793

794  $\alpha + \sum_{k=2}^K \gamma_k 1(G_c = g_k) + \kappa E + \sum_{t=2}^M \omega_t 1(D_c = D_t)$  (Eq. 17)

795

796 where  $G$  is the index of cell type,  $E$  is the experimental time index (0, 1, 2 corresponds to control,  
797 1h, and 6h after treatment, respectively), and  $D$  is the donor index. The null hypothesis for the test  
798 is  $H_0: \kappa = 0$ .

799

800 Gene and pathway enrichment with GREAT

801 We used the GREAT method (v. 4.0.4) to conduct gene and enrichment analysis<sup>34</sup>, with DARs as  
802 input and default parameter settings. The output from GREAT for the human PBMC data can be  
803 found in the **Supplementary Tables 17-18**.

804

805 **Figure legends:**

806

807 **Figure 1. PACS modeling framework.**

808 Upper panel: Illustration of the latent accessibility of cells. Multiple factors including cell types,  
809 developmental stages, spatial locations etc. determines the chromatin structure and configurations  
810 of corresponding cell groups. These different chromatin structures result in the variable Tn5  
811 insertion rates in the ATAC-seq experiments. The readout of ATAC assays are paired insertion  
812 counts (PIC), which are crude measures of latent insertion rates.

813 Lower panel: Illustration of the sequencing reads capturing process of snATAC-seq. During PCR  
814 and sequencing, fragments in each single cell are partially captured, and after data processing,  
815 variable capturing probability should be accounted for in data modeling.  
816

817 **Figure 2. Parameter estimation evaluation and application to cell type annotations.**

818 **a-d.** Parameter estimation accuracy evaluated using simulation data. Here p represents  $P(y \geq 1)$   
819 and q represents the capturing probability. For this panel and all panels below, the error bars  
820 indicate the standard deviation across repeated simulations ( $n=5$ ).

821 **e.** Comparison of cell type annotation adjusted rand index (ARI) between PACS and Naïve Bayes  
822 method.

823 **f.** Confusion matrix between true cell type labels and PACS-inferred cell type labels for the human  
824 cell line mixture data (low cell loading setting). The confusion matrices for other datasets are in  
825 the Supplementary Figure 1.

826 **g.** Confusion matrix between true cell type labels and Naïve Bayes-inferred cell type labels for the  
827 human cell line mixture data (low cell loading setting).

828

829 **Figure 3. Compound hypothesis testing with PACS is sensitive and specific.**

830 **a-b.** Type I error and power evaluation using single-factor simulation data.

831 **c-d.** Type I error and power evaluation using two-factor simulation data. Methods with “-n”  
832 represents the setting of Naïve test, where other factors are ignored when testing the factors of  
833 interest. Methods ending with “-s” represent the stratified test where we stratify on other factors  
834 and test the factors of interest within the strata.

835 **e.** Illustration of linear and quadratic effects of treatment on accessibility across time points. Effect  
836 sizes are defined as the fold change between the highest accessibility over the lowest accessibility,  
837 across five time points.

838 **f.** Evaluation of power in detecting linear and quadratic temporal effects using simulated data with  
839 different effect sizes.

840 **g-h.** Type I error and power evaluation using empirical adult mouse kidney data.

841

842 **Figure 4. Application of PACS to the mouse kidney dataset.**

843 **a-b.** UMAP dimension reduction plot constructed with all features (a) or after excluding features  
844 with significant batch effect (b), colored by batch labels. Features with batch effect are detected  
845 with PACS differential test module, and FDR multiple testing correction is applied.  
846 **c-d.** UMAP dimension reduction plot constructed with all features (a) or after removing features  
847 with batch effect (b), colored by cell types.  
848 **e.** IGV plot of peak summits around cell type-specific genes identified by PACS, for PCT and PST  
849 cell types. The list of cell type specific genes is generated with GREAT enrichment analysis using  
850 differentially accessible peaks.  
851 **f.** Heatmap of normalized gene expression z scores for the scRNA-seq data from male (-m) and  
852 female (-f) kidneys. The list of genes match those from the panel **f**.  
853

854 **Figure 5. Application of PACS to the developing human brain data.**  
855 **a.** Illustration of the developing human brain dataset. The subset of data we analyzed are composed  
856 of samples from three donors across six brain anatomical regions, and we focused on the excitatory  
857 neuron lineage.  
858 **b-c.** UMAP visualization of the data complexity, with points colored by cell type (b) or anatomical  
859 regions (c). RG, radial glia; IPC, intermediate (neuro-) progenitor cells; earlyEN, early excitatory  
860 neurons; dLEN, deep layer excitatory neurons; uLEN, upper layer excitatory neurons; M1, primary  
861 motor cortex; Parietal, dorsolateral parietal cortex; PFC, dorsolateral prefrontal cortex; Somato,  
862 primary somatosensory cortex; Temporal, temporal cortex; V1, primary visual cortex.  
863 **d.** Motif enrichment results for PFC- and V1-specific peaks identified using PACS. PWM, position  
864 weight matrix.  
865 **e.** Accessibility z score of PFC and V1 peaks across five cell types.  
866

867 **Figure 6. Application of PACS to time-series dataset from human PBMC treatment data.**  
868 **a.** Factor landscape of the PBMC treatment dataset. Here, another layer of factor is the four  
869 different treatments, which can also be jointly considered in the model, but for demonstration  
870 purposes, we only focus on the PMA treatment effect. The control time point is considered as time  
871 0, and the times of one and six hours after treatment are considered as time 1 and 2, respectively.  
872 **b-c.** Summary of significant up- or down- regulated peaks after PMA treatment for each cell type.

873 **d-e.** Heatmap of significant up- or down- regulated peaks after PMA treatment, grouped by time  
874 point and cell type. The color scale (scaled\_acc) represents the accessibility z score.

875

876 **Supplementary Figure 1.**

877 **a-b.** Parameter estimation accuracy evaluated using simulation data. Here p represents  $P(y \geq 1)$   
878 and q represents the capturing probability. For this panel and all panels below, the error bars  
879 indicate the standard deviation across repeated simulations ( $n=5$ ).

880 **c-j.** Confusion matrix between true cell type labels and PACS-inferred (or Naïve Bayes-inferred)  
881 cell type labels for four datasets.

882

883 **Supplementary Figure 2.**

884 **a-e.** Quantile-quantile plots for P values under the null for five testing methods, using simulated  
885 data with no insertion rate difference.

886 **f-i.** Type I error and power evaluation using empirical cell line mixture data or marmoset brain  
887 data.

888

889 **Supplementary Figure 3.**

890 **a-b.** UMAP dimension reduction plot constructed after excluding features with significant batch  
891 effect ( $P$  value  $< 0.05$ , no FDR correction), colored by batch labels (a) or cell types (b). Features  
892 with batch effect are detected with PACS differential test module.

893

894 **Supplementary Figure 4.**

895 **a.** UMAP dimension reduction plot constructed with all features, colored by batch labels. This  
896 panel is identical to **Fig. 4a**, and is displayed here for examining feature plots in panels **b-l**.

897 **b-l.** Feature plots for top significant batch effect peaks determined by PACS.

898

899 **Supplementary Figure 5.**

900 **a-c.** Violin plots that summarize number of fragments in each cell across different donors (a), brain  
901 regions (b), or cell types (c), for the human brain data.

902

903

904 **Supplementary Materials:**

905

906 Supplementary Figures 1-5

907 Supplementary Table 1: Parameter estimation using simulated data

908 Supplementary Table 2: Type 1 error and power of different methods using simulated data (one-factor setting)

910 Supplementary Table 3. Type 1 error and power of different methods using simulated data (two-factor setting)

912 Supplementary Table 4. PCT specific peaks in the adult kidney data

913 Supplementary Table 5. PST specific peaks in the adult kidney data

914 Supplementary Table 6. GREAT gene enrichment results of PCT specific peaks

915 Supplementary Table 7. GREAT gene enrichment results of PST specific peaks

916 Supplementary Table 8. Number of cells in across spatial regions and donors

917 Supplementary Table 9. V1 specific peaks in the developing human brain data

918 Supplementary Table 10. PFC specific peaks in the developing human brain data

919 Supplementary Table 11. Homer motif enrichment results of the V1 region in the human developing brain data

921 Supplementary Table 12. Homer motif enrichment results of the PFC region in the human developing brain data

923 Supplementary Table 13. Number of differential peaks between PFC and V1 across excitatory neuron lineage in the developing human brain data

925 Supplementary Table 14. Significant up-regulated peaks after treatment across cell types in the PBMC treatment data

927 Supplementary Table 15. Significant down-regulated peaks after treatment across cell types in the PBMC treatment data

929 Supplementary Table 16. Number of significant differential peaks after treatment across five cell types, using PACS or ArchR

931 Supplementary Table 17. GREAT pathway enrichment results of up-regulated treatment effect peaks in T cells

933 Supplementary Table 18. GREAT gene enrichment results of up-regulated treatment effect peaks in T cells

935

## 936 **Code Availability**

937 PACS is an open-access software available at the GitHub repository [https://github.com/Zhen-](https://github.com/Zhen-Miao/PACS)  
938 [Miao/PACS](https://github.com/Zhen-Miao/PACS). Codes for reproducing the analyses are also available at the GitHub page.

939

## 940 **Author Contribution**

941 JK and ZM conceived the study. ZM, JW, and JK designed the statistical model. JW formulated  
942 the missing data model for sequencing depth and derived the analytical expression for missing-  
943 corrected logistic regression estimation procedure. ZM implemented the model and constructed  
944 the software package with feedback from JW, DK, and JK. ZM conducted the simulation and real  
945 data analysis with help from KP and DK. JK supervised the work. JK and ZM wrote the manuscript  
946 with feedback from JW.

947

## 948 **Acknowledgements**

949 This work has been supported in part by the UC2DK126024 grant to JK and also by the Health  
950 Research Formula Fund of the Commonwealth of Pennsylvania who did not play a direct role in  
951 the work. We thank Blavatnik Family Fellowship that supported the work of ZM. We thank Dr.  
952 Pablo Camara, Dr. Nancy Zhang, Dr. Kui Wang, Dr. Xiangjie Li, Dr. Yinan Lin, Dr. Mengying  
953 You and members of Junhyong Kim's lab, especially Erik Nordgren for their constructive  
954 suggestions that improved this work. We thank Dr. Kun Zhang and Dr. Jason Buenrostro for  
955 sharing the metadata.

956

## 957 **Competing interests**

958 The authors declare no competing interest.

Fig. 1

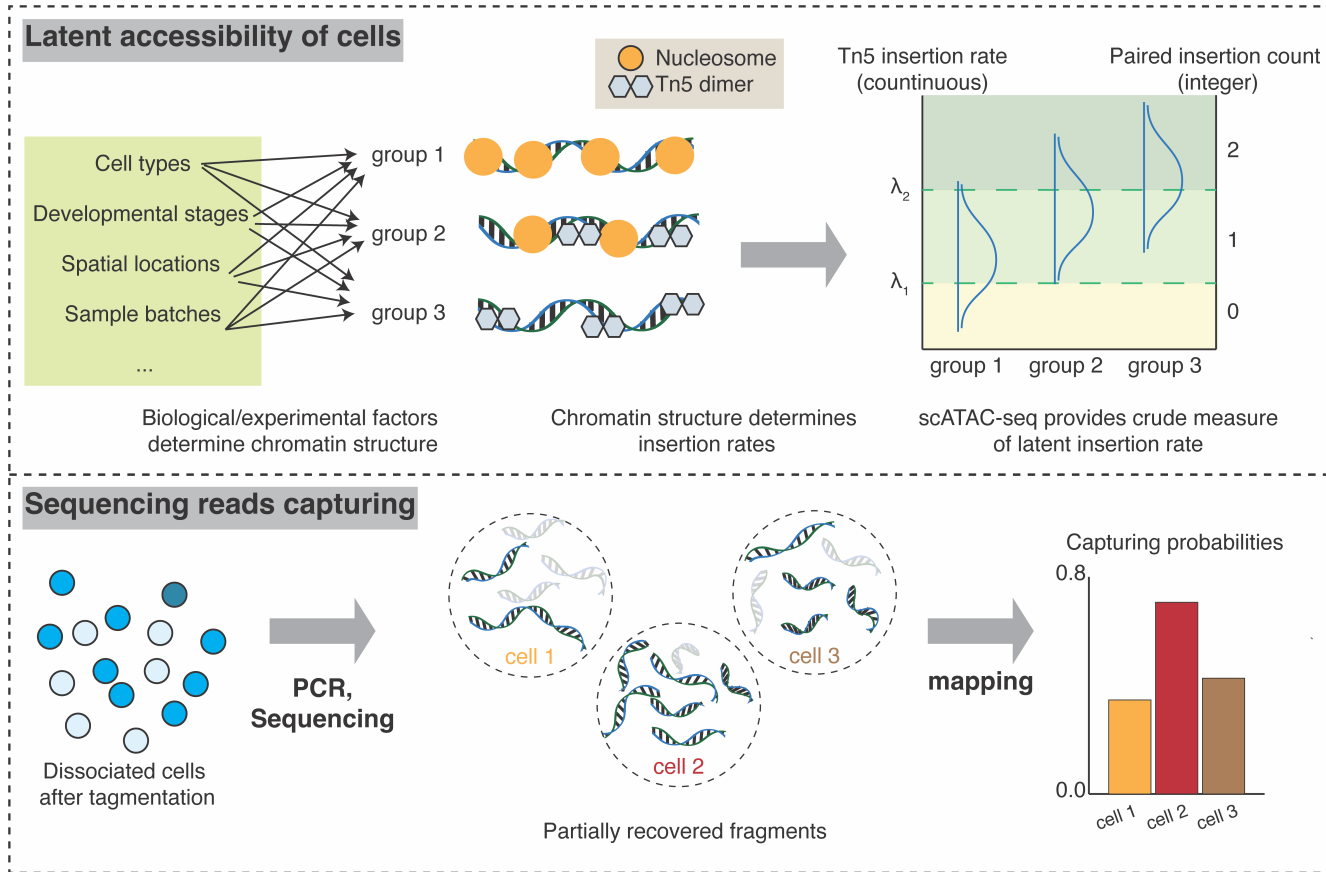


**Fig. 2**

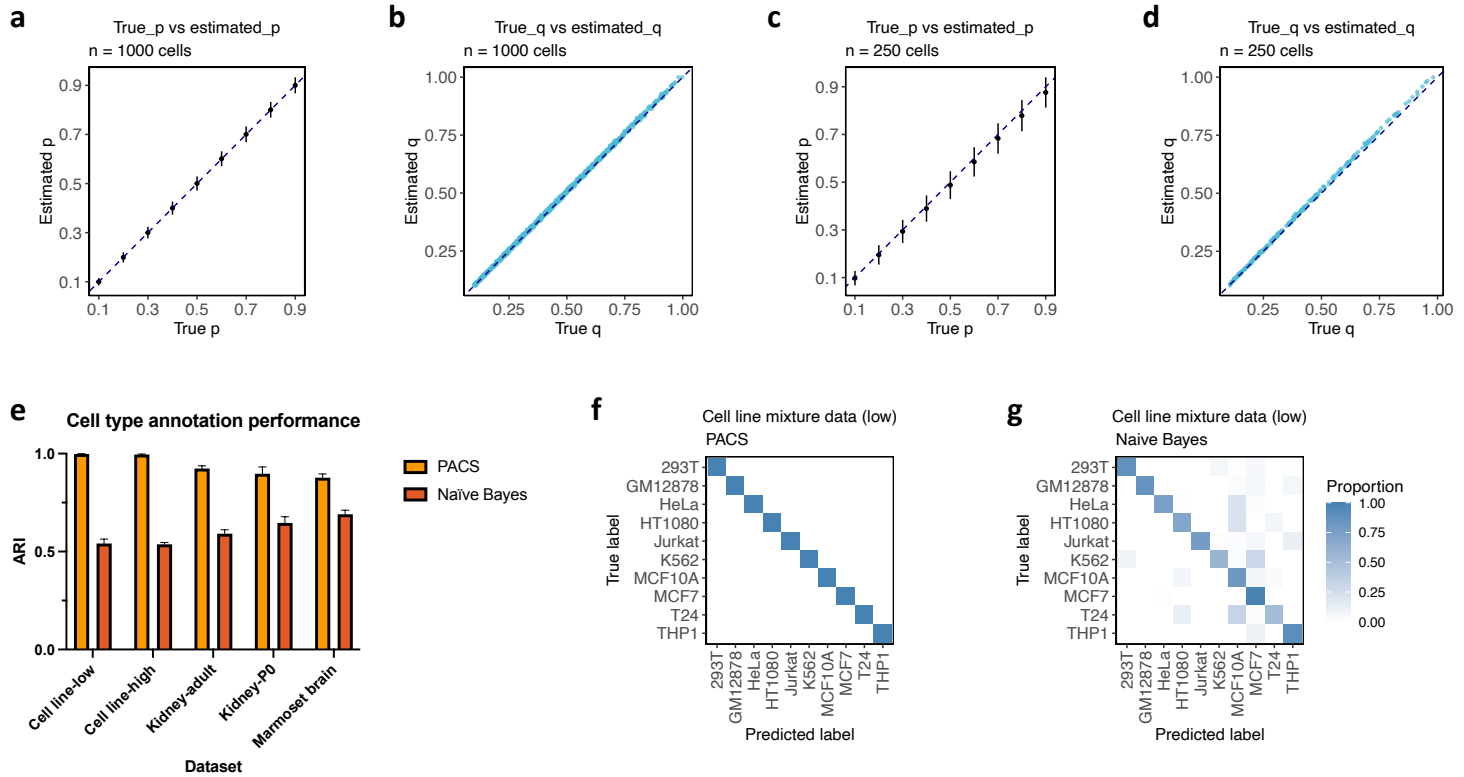


**Fig. 3**

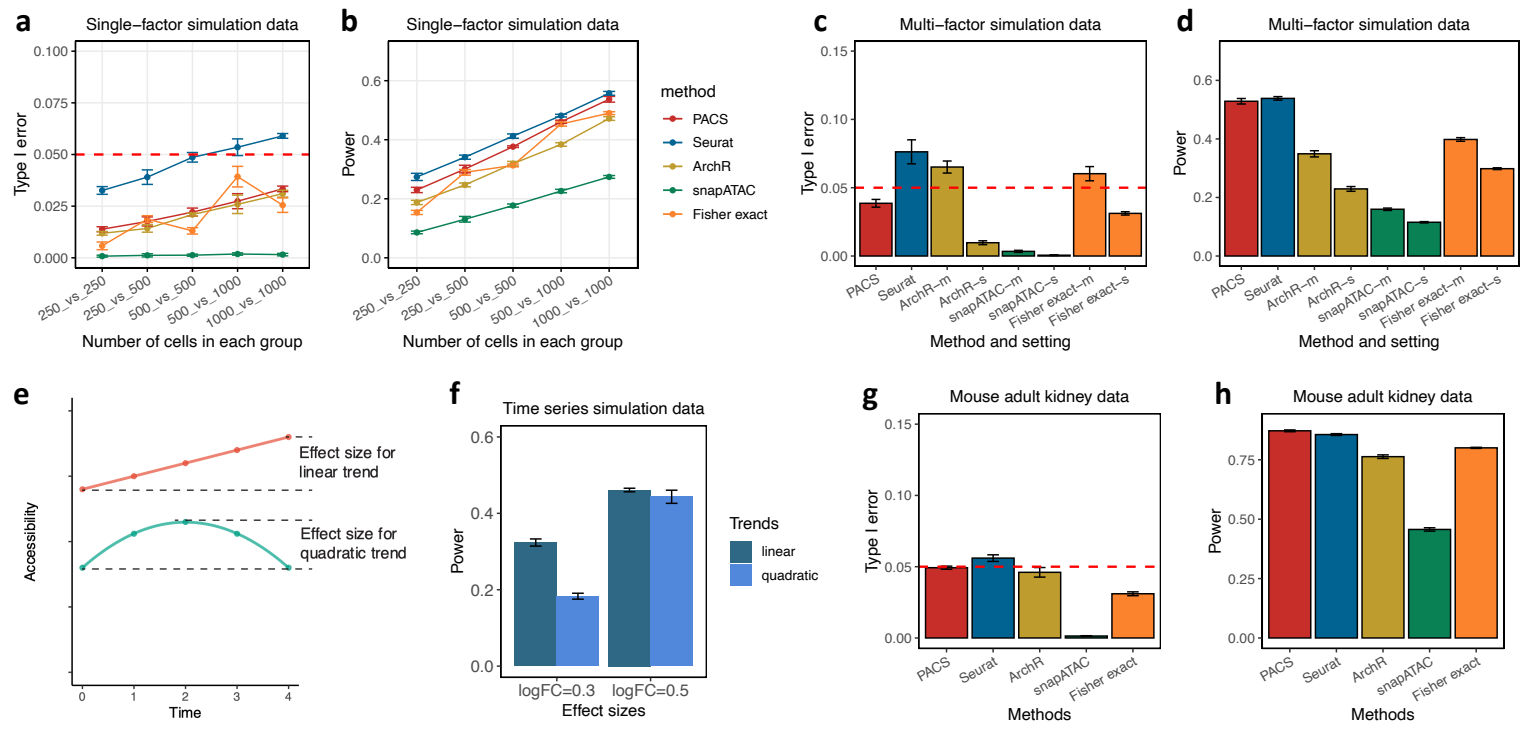


**Fig. 4**

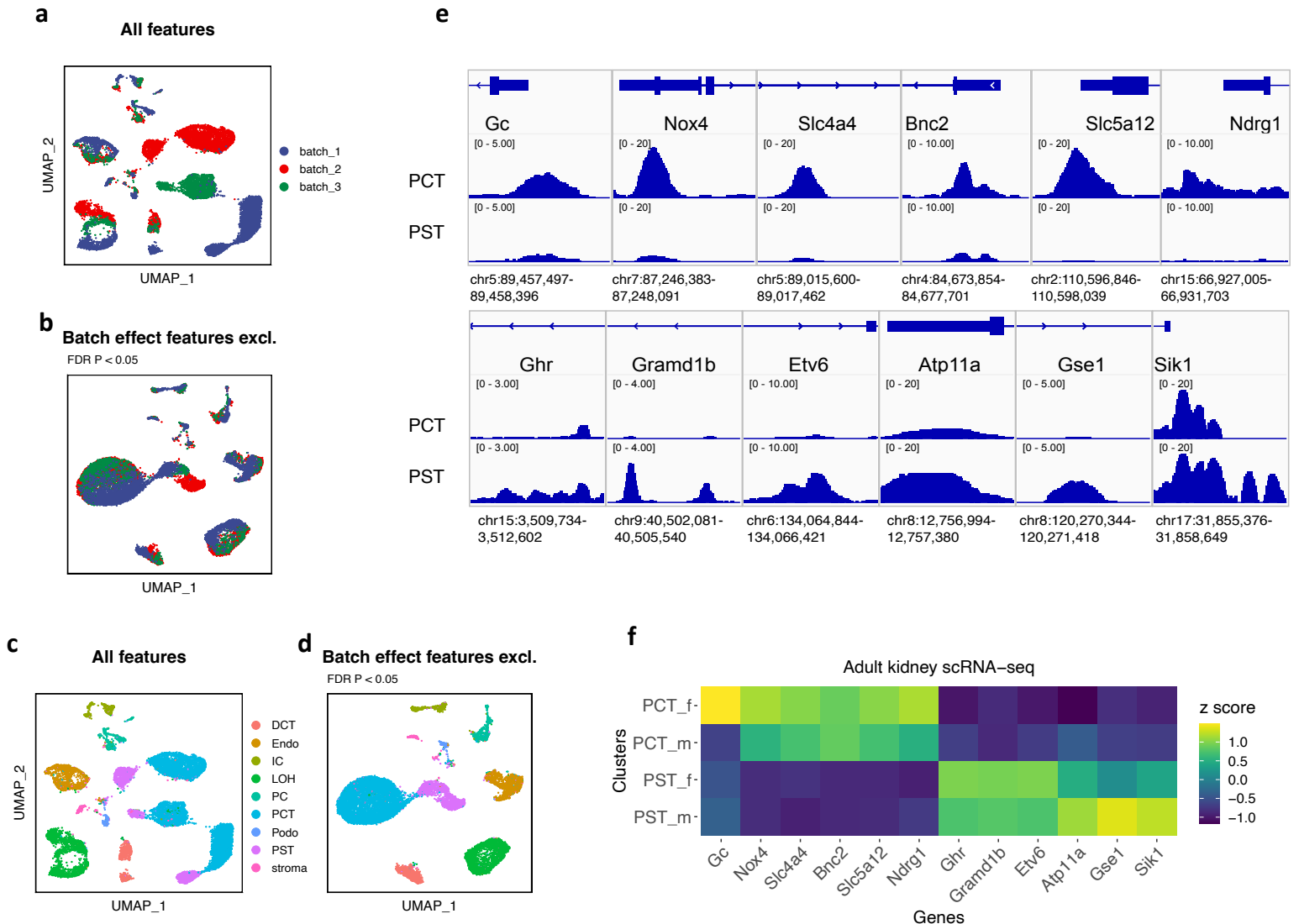


**Fig. 5**

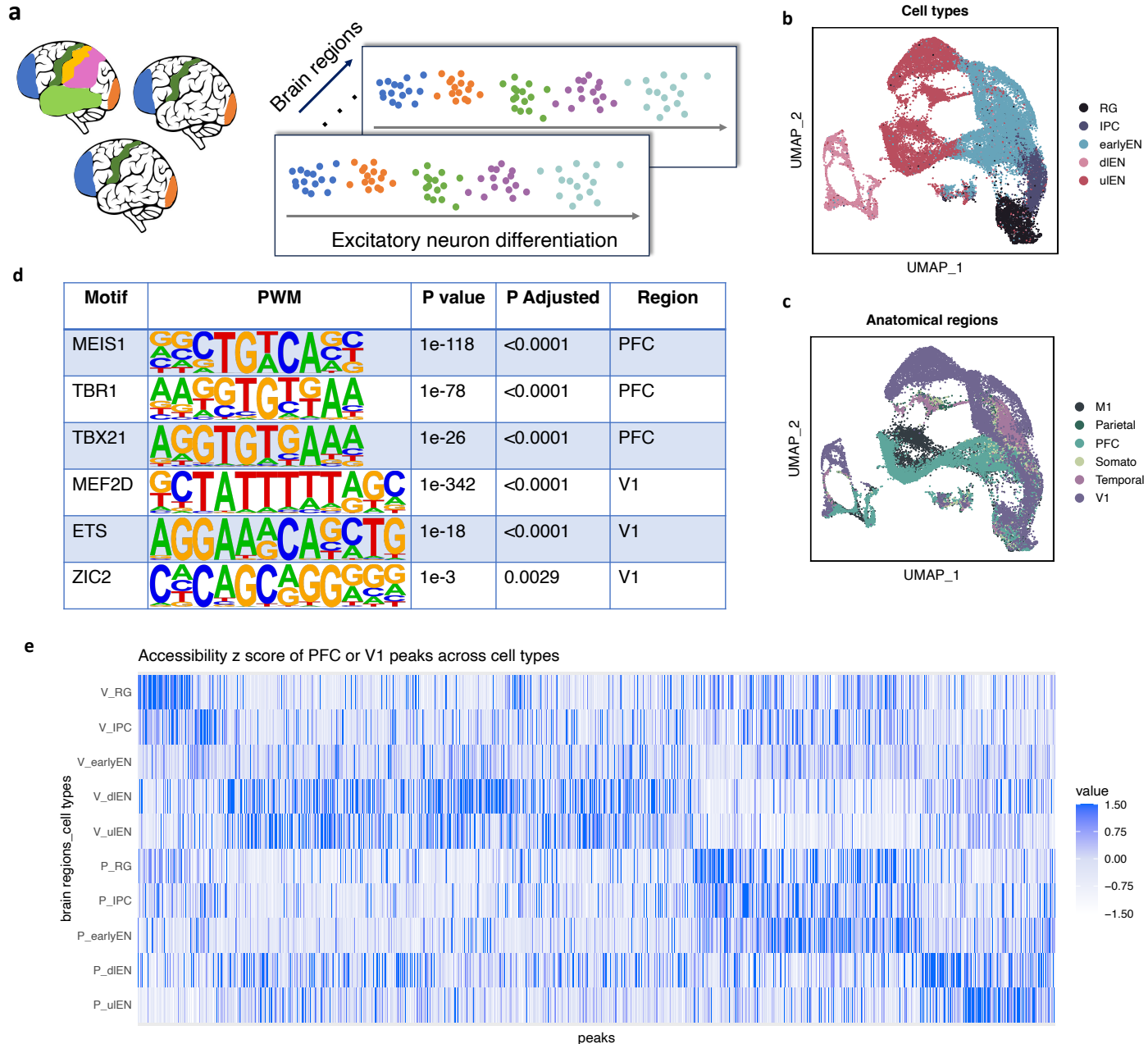


**Fig. 6**

